Center for Turbulence Research
Proceedings of the Summer Program 2018

Using particle-resolved LES to improve Eulerian-Lagrangian modeling of shock-wave/particle-cloud interactions

By M. Vartdal† AND A. N. Osnes‡

We perform particle resolved large-eddy simulations of a shock wave passing through a random array of stationary particles, varying incident shock Mach number, particle number density and volume fraction. The variation of the mean flow is quantified by fitting the reflected and transmitted shock wave Mach numbers as power laws of these parameters. We analyze the fluctuations from locally volume averaged quantities, and find that the fluctuating kinetic energy is generated primarily by the forces on the particles, and reaches values as high as two thirds of the mean kinetic energy. We use the data from the particle-resolved simulations to close the volume averaged equations, in which the present problem can be formulated in one dimension, and demonstrate that correct drag laws and sub-grid closures are necessary for reliable predictions.

1. Introduction

The interaction of a shock wave with a cloud of particles is a canonical high speed multiphase flow problem that has recently received some attention in both numerical (Houim & Oran 2016) and experimental studies (Ling *et al.* 2012; Theofanous *et al.* 2016). Interactions of this type play an important role in several applications of practical interest, such as explosive blast mitigation, design of combustion systems and atmospheric dissemination of powders and liquids. Resolved simulations of such systems are typically not possible due to the extremely large scale separations. This means that appropriate model equations are needed in order to provide useful predictions.

A particularly challenging case is high-speed particle laden flows with moderate particle volume fractions, i.e. ranging from 1% to 10-15%, as the models employed for either low or high volume fractions are inapplicable, and a model for the intermediate regime has not yet been established. A number of studies have considered either Eulerian-Eulerian models or Eulerian-Lagrangian models for the intermediate regime, but in the past these have had a number of issues. Careful derivation of the model equations are needed to ensure that the equations are well posed (Lhuillier *et al.* 2013; McGrath *et al.* 2016), and additionally the models might be missing important physical processes which are crucial in order to obtain correct particle distributions (Theofanous & Chang 2017).

Recently, a few studies have considered resolved simulations of shock-wave particle-cloud interactions to investigate the particle scale physics in order to improve the simplified models. The Euler equations were employed in resolved simulations with both structured arrays (Mehta *et al.* 2016) and random arrays (Mehta *et al.* 2018). Regele *et al.* (2014) and Hosseinzadeh-Nik *et al.* (2018) considered viscous two-dimensional simulations of shock waves passing through arrays of cylinders and examined the genera-

† Norwegian Defence Research Establishment, Norway
‡ Institute of Technology Systems, University of Oslo, Norway

tion of vorticity by baroclinic torque and vorticity-dilatation. Theofanous *et al.* (2018) considered an effective boundary method for the Euler equations and obtained particle distribution results in good agreement with experiments. The current work extends the previous studies by performing particle-resolved LES simulations of a shock-wave passing through a particle-cloud and quantifying the particle scale fluctuations. Specifically, we generate datasets containing all the terms in the volume averaged equations of motion, including the equation for the fluctuating kinetic energy. We vary the incident shock wave Mach number, particle number density and volume fraction. The resulting dataset spans a parameter space that has not been explored in any other study. Furthermore, we develop a closure of the volume averaged equations in an attempt to improve the predictive capability of the Eulerian-Lagrangian models for the statistically 1D configuration. The proposed closure consists of an additional equation for the unresolved kinetic energy and a turbulence length scale.

2. Governing equations and computational method

In the following, $\bar{\cdot}$ denotes a volume averaged quantity, $\langle\cdot\rangle$ denotes a phase averaged quantity and $\tilde{\cdot} = \langle\rho\cdot\rangle/\langle\rho\rangle$ denotes a Favre-averaged quantity. The volume and phase average of continuous phase quantities are related by $\alpha\langle\cdot\rangle = \bar{\cdot}$, where α is the continuous phase volume fraction. We utilise both Reynolds and Favre decomposition, where we use the notation $u_i = \langle u\rangle_i + u'_i$ for the former and $u_i = \tilde{u}_i + u''$ for the latter. The Favre- and Reynolds averaged velocities are related by $\tilde{u}_i - \langle u\rangle_i = a_i$, where $a_i = -\langle u''\rangle_i = \langle\rho' u'_i\rangle/\langle\rho\rangle$ is commonly referred to as the turbulent mass flux. For a description of the volume averaging procedure, including the effects of density fluctuations, consult Schwarzkopf & Horwitz (2015). We use subscripts IS, RS and TS to refer to quantities related to the incident shock, reflected shock and transmitted shock, respectively.

2.1. *Governing equations*

The resolved simulations in this work are described by the conservation equations for mass, momentum and energy. These are expressed in differential form as

$$\partial_t\rho + \partial_k(\rho u_k) = 0, \tag{2.1}$$

$$\partial_t(\rho u_i) + \partial_k(\rho u_i u_k) = -\partial_i p + \partial_j\sigma_{ij}, \tag{2.2}$$

$$\partial_t(\rho E) + \partial_k(\rho E u_k + p u_k) = \partial_j(\sigma_{ij}u_i) - \partial_k(\lambda\partial_k T), \tag{2.3}$$

where ρ is the mass density, u is the velocity, p is the pressure, $\sigma_{ij} = \partial_j[\mu(\partial_j u_i + \partial_i u_j - 2\partial_k u_k\delta_{ij}/3)]$ is the viscous stress tensor, μ is the dynamic viscosity, $E = \rho e + 0.5\rho u_k u_k$ is the total energy per unit mass, e is the internal energy per unit mass, λ is the thermal conductivity, and T is the temperature. The system of equations is closed by an ideal gas equation of state, a constant specific heat capacity, a power law dependence of viscosity on temperature with an exponent of 0.76, and a Prandtl number of 0.7. The pre-shock state is air at standard conditions.

In the statistically one-dimensional cases considered here, the application of volume averaging to the governing equations, assuming stationary inert particles, yields

$$\partial_t(\alpha\langle\rho\rangle) + \partial_x(\alpha\langle\rho\rangle\tilde{u}_0) = 0, \tag{2.4}$$

$$\partial_t \left(\alpha\langle\rho\rangle\tilde{u}_0\right) + \partial_x \left(\alpha\langle\rho\rangle\tilde{u}_0\tilde{u}_0 + \alpha\langle p\rangle\right) = \partial_x \left(\alpha\langle\sigma\rangle_{00}\right) - \partial_x \left(\alpha\langle\rho\rangle\tilde{R}_{00}\right) + \frac{1}{V}\int_S p n_0 dS - \frac{1}{V}\int_S \sigma_{0k} n_k dS, \tag{2.5}$$

$$\partial_t \left(\alpha\langle\rho\rangle\tilde{E}\right) + \partial_x \left(\alpha\langle\rho\rangle\tilde{E}\tilde{u}_0 + \alpha\langle p\rangle\tilde{u}_0\right) = \partial_x \left(\alpha\langle\sigma_{00}\rangle\tilde{u}_0\right) - \partial_x \left(\alpha\langle\lambda\partial_x T\rangle\right) - \partial_x \left(\alpha\langle\rho e'' u_0''\rangle\right) - \partial_x \left(\alpha\langle\rho\rangle\tilde{R}_{00}\tilde{u}_0\right) + D^u + D^p + D^\mu + D^{ap} + D^{a\mu}. \tag{2.6}$$

Here, $\tilde{R}_{00} = \widetilde{u_0'' u_0''}$ is a turbulent stress analogous to the classical Reynolds stresses, V denotes the averaging volume, $D^u = -1/2\partial_x \left(\alpha\langle\rho u_i'' u_i'' u_0''\rangle\right)$ is the turbulent diffusion, $D^p = -\partial_x \left(\alpha\langle p' u_0'\rangle\right)$ is the pressure diffusion, $D^\mu = \partial_x \left(\alpha\langle u_j' \sigma_{j0}'\rangle\right)$ is the viscous diffusion, $D^{ap} = \partial_x \left(\alpha a_0 \langle p\rangle\right)$ is the pressure-diffusion effect due to the density-velocity correlation, $D^{a\mu} = -\partial_x \left(\alpha a_0 \langle\sigma\rangle_{00}\right)$ is the analogous viscous diffusion effect and S denotes the continuous phase boundary. For discussion purposes we also define the mean kinetic energy per unit mass $\tilde{K} = 0.5\tilde{u}_k\tilde{u}_k$.

The 1D volume averaged model includes a transport equation for the fluctuating kinetic energy, $k = 0.5\widetilde{u_k'' u_k''}$, which is of the form

$$\partial_t \left(\alpha\langle\rho\rangle k\right) + \partial_x \left(\alpha\langle\rho\rangle\tilde{u}_0 k\right) = D^u + D^p + D^\mu + D^{ap} + D^{a\mu} + P + M^p + M^\mu + \Pi - \varepsilon + A + B, \tag{2.7}$$

where $P = -\alpha\langle\rho\rangle\tilde{R}_{00}\partial_x\tilde{u}_0$ is a production term due to velocity gradients, $\varepsilon = \alpha\langle\sigma_{jk}'\partial_k u_j'\rangle$ is the viscous dissipation, $M^p = -\alpha\langle p\rangle\partial_x a_0$ is a pressure driven production term due to divergence of the density-velocity correlation, $M^\mu = \alpha\langle\sigma\rangle_{00}\partial_x a_0$ is the analogous viscous production term, and $\Pi = \alpha\langle p'\partial_k u_k'\rangle$ is the pressure-dilatation correlation. This leaves

$$A = -\frac{\tilde{u}_0}{V}\int_S p n_k dS, \qquad B = \frac{\tilde{u}_0}{V}\int_S \sigma_{jk} n_k dS, \tag{2.8}$$

which are the production due to the pressure and viscous forces on the particles, respectively.

2.2. *Computational method*

The resolved simulations are performed using the CharLES solver from Cascade Technologies (Bres *et al.* 2018). It is an entropy-stable Voronoi-mesh based solver with third order Runge-Kutta based time-stepping. For the one-dimensional simulations, we use an in-house code that solves Eqs. (2.4)-(2.7). It uses first order reconstruction of primitive variables at the control-volume faces and the fluxes are computed using a Lax-Friedrich type method. Time-stepping is computed by a third order Runge-Kutta scheme. The closure models used for the numerous unclosed terms in Eqs. (2.4)-(2.7) will be discussed below.

3. Resolved simulations

We have simulated the passage of a shock wave through particle clouds of volume fractions in the range $\alpha \in [0.05, 0.1]$. Figure 1 shows a sketch of the problem setup. The particle cloud is located between $x/L = 0$ and $x/L = 1$, where $L = 1.94088 \times 10^{-3}$ m, and the span-wise extent is $L_y = L_z = 2L/3$ for the cases with the largest particle

Case	Ma	r	α_p	$Re_\mathrm{p,IS}$	n [mm^{-3}]	D_p [μm]	$\Delta p_\mathrm{RS}/p_\mathrm{IS}$	$\Delta p_\mathrm{TS}/p_\mathrm{atm}$	Ma_RS	Ma_TS
I	2.2	1.235	0.1	6160	191.0	100	0.9103	2.948	1.334	1.878
II	2.4	1.235	0.1	7091	191.0	100	1.127	3.593	1.402	2.020
III	2.6	1.235	0.1	7927	191.0	100	1.334	4.279	1.464	2.160
IV	2.8	1.235	0.1	8666	191.0	100	1.527	5.053	1.519	2.309
V	3.0	1.235	0.1	9309	191.0	100	1.700	5.900	1.567	2.461
VI	2.6	1.445	0.1	6292	382.0	79.4	1.365	3.881	1.473	2.080
VII	2.6	1.726	0.1	4994	763.9	63.0	1.396	3.582	1.482	2.018
VIII	2.6	1.903	0.075	4537	763.9	57.2	1.313	3.957	1.458	2.096
IX	2.6	2.180	0.05	3964	763.9	50	1.160	4.486	1.412	2.201
X	2.2	2.097	0.1	3080	1528	50	0.9908	2.261	1.360	1.714
XI	2.6	2.097	0.1	3964	1528	50	1.429	3.313	1.492	1.960
XII	3.0	2.097	0.1	4654	1528	50	1.803	4.669	1.596	2.236

TABLE 1. The different simulations considered in this study and key parameters. $Re_\mathrm{p,IS}$ is the particle Reynolds number based on post incident shock values, and n is the number density.

diameters. We keep the ratio of span-wise extent to particle diameter constant for all the simulations. The position of the spheres are drawn randomly, with a minimum distance between the sphere centers of 1.5 D_p and a minimum distance between the spheres and the boundaries of $D_\mathrm{p}/20$. We use body fitted structured meshes around each sphere extending $D_\mathrm{p}/5$ out from the particle surface. These body fitted meshes have 10 points in the sphere normal direction with a growth ratio of approximately 1.1. The rest of the computational mesh is a Voronoi mesh with approximately uniform density matching the outer cell dimensions of the body fitted meshes. The overall mesh consists of 50-70 million cells depending on the number of particles involved. No-slip boundary conditions are applied on the particles and slip elsewhere. A grid-sensitivity test was conducted with twice and half the number of points for $Ma = 3$, $\alpha_\mathrm{p} = 0.1$ and $D_p = 100$ μm, and the results were not found to be grid-sensitive within this range.

The statistics of the flow are quantified by computing a moving volume average. The averaging volume extends $\sqrt[3]{4}D_\mathrm{p,max}$ in the streamwise direction and span both lateral directions, where $D_\mathrm{p,max}$ is the largest particle diameter considered in this study. This gives a minimum of 50 particles per averaging volume.

The general flow structure is the same for all cases considered. Figure 2 shows the position of the incident, transmitted and reflected shock waves, upstream and downstream contact lines and acoustic waves emanating from $x/L = 0.25$, $x/L = 0.5$, $x/L = 0.75$, $x/L = 0.98$ and $x/L = 1$ for case VII. Time is non-dimensionalised by $\tau_L = L/u_\mathrm{IS}$, which is the time it takes for the shock to travel a distance equal to the particle cloud length. The transmitted shock is attenuated as it passes through the particle cloud, while the reflected shock is strengthened continuously over the time-frame considered here. The acoustic wave emanating from $x/L = 0.98$ can be seen to have an infinite slope, which indicates that the flow chokes at this point and becomes supersonic further downstream, as can be seen by the acoustic wave emanating at $x/L = 1$. There is also a quasi-stationary shock downstream of the particle cloud, but this shock is very irregular and takes some time to develop, thus it is not shown in the figure.

The different simulations and key parameters describing the bulk behavior are shown in Table 1. Ma_RS and Ma_TS are the average shock wave Mach numbers of the reflected shock between $x/L = -0.2$ and $x/L = -0.01$, and the transmitted shock between $x/L = 1$

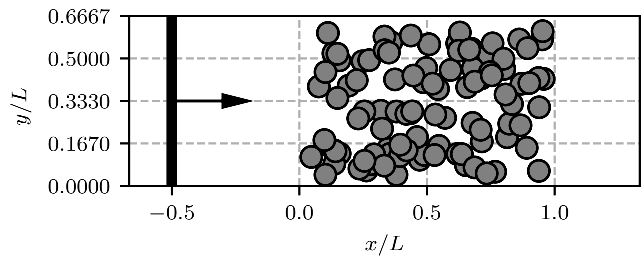

FIGURE 1. Sketch of the 3D simulation problem setup. A shock wave, shown in the left part of the figure passes through the cloud of particles located between $x/L = 0$ and $x/L = 1$.

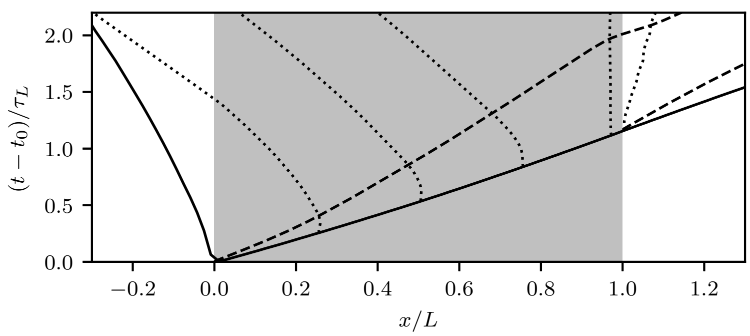

FIGURE 2. Wave diagram showing the positions of the incident, transmitted and reflected shock waves (solid lines), upstream and downstream contacts (dashed lines) and acoustic waves (dotted lines) in case VII. The particle cloud is indicated by the grey region.

and $x/L = 1.3$, respectively. With increasing incident shock wave Mach number we see a strengthening of both the reflected and transmitted shocks. Increasing the theoretical mean minimal particle separation,

$$r = \frac{1}{N_\mathrm{p} D_\mathrm{p}} \sum_p \min_{\forall i \neq p} ||x_i - x_p||, \tag{3.1}$$

which is a non-dimensional measure of number density, increases the reflected shock strength and decreases the transmitted shock strength. Decreasing particle volume fraction increases Ma_{TS} and decreases Ma_{RS}. We fit the reflected and transmitted shock Mach numbers as power laws of incident shock Mach number, r and volume fraction. The resulting functions are

$$Ma_{\mathrm{RS}} = 1.035 \alpha_\mathrm{p}^{0.0768} r^{0.03865} Ma^{0.5395}, \tag{3.2}$$

and

$$Ma_{\mathrm{TS}} = 0.6566 \alpha_\mathrm{p}^{-0.1726} r^{-0.1813} Ma^{0.8716}. \tag{3.3}$$

In addition to the dependencies described above, the strength of the transmitted and reflected shocks depend in a non-trivial manner on the regularity of the particle distribution (Mehta *et al.* 2016, 2018).

To estimate the importance of the velocity fluctuations, we consider the ratio of fluctuating kinetic energy to mean kinetic energy. Figure 3 shows the ratio of fluctuating kinetic energy to total kinetic energy for $(t - t_0)/\tau_L = 0.5,\ 1$ and 2, where t_0 is the time when the incident shock impacts the particle cloud. Clearly, k contains a significant amount of

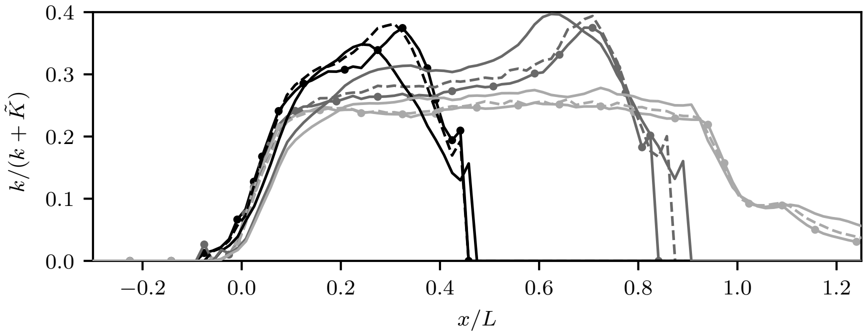

FIGURE 3. Ratio of fluctuating kinetic energy to total kinetic energy at $(t-t_0)/\tau_L = 0.5$ (black), 1, (grey) and 2 (light grey). Solid lines: case III, dashed lines: case VII, solid line and disks: case XI.

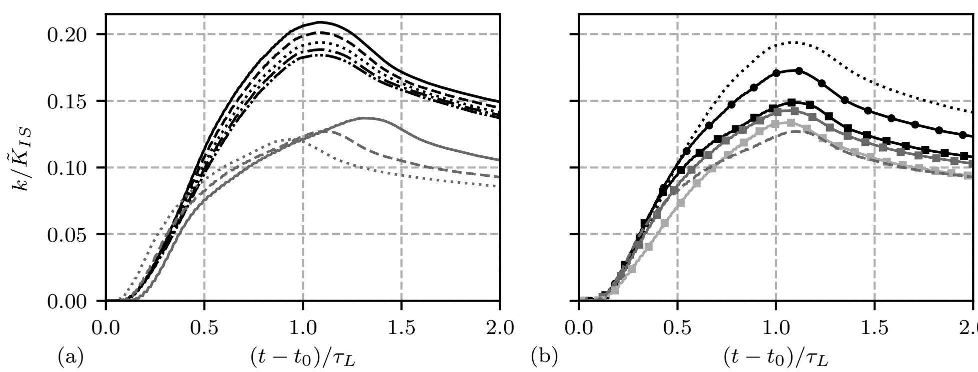

FIGURE 4. Mean fluctuating kinetic energy over $x/L = 0.1$ to $x/L = 0.9$. Solid black line: case I, black dashed line: case II, black dotted line: case III, black dash-dotted line: case IV, black dashed and double-dotted line: case V, black line and circles: case VI, black squares: case VII, dark grey squares: case VIII, light grey squares: case IX, grey solid line: case X, grey dashed line: case XI, grey dotted line: case XII.

the kinetic energy, peaking at about 2/3 of $\tilde{K}$. We observe that k peaks a few particle diameters behind the primary shock wave, and subsequently decays to a value that stays roughly constant throughout the particle cloud. Figure 4(a) shows the mean fluctuating kinetic energy over $x/L = 0.1$ to $x/L = 0.9$ normalised by the kinetic energy behind the incident shock for the cases with $n = 191$ mm^{-3} and those with $n = 1528$ mm^{-3}. The average value peaks after the shock has passed through the particle cloud, and for the largest particle size the timing of the peak value collapses when scaled by τ_L. For the smallest particles, we observe that the timing of the peak does not collapse with the shock-associated time scale, and that the peak is earlier for the higher Mach numbers. The normalised fluctuating kinetic energy magnitude can be seen to decrease with Mach number, but this should not be confused with a decrease in absolute values of the fluctuation intensity. A similar plot for the cases with $Ma = 2.6$ is shown in Figure 4(b). We note that the timing of the peak does not collapse when scaled by τ_L here either, but the deviation is small. Higher number densities (or r) result in a delayed and smaller peak value. As a higher number density corresponds to a larger particle surface area within the particle cloud, we could expect more intense fluctuations, since (as will be shown below)

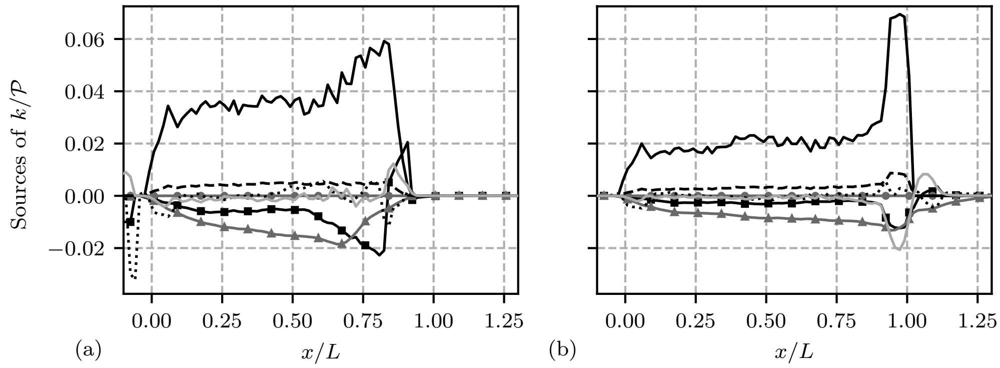

FIGURE 5. Source terms in Eq. (2.7) for case VII at (a) $(t-t_0)/\tau_L = 1$ and (b) $(t-t_0)/\tau_L = 2$, non-dimensionalised by $\mathcal{P}$. Black solid line: A, black dashed line: B, grey solid line and triangles: ε, black solid line and squares: Π, black dotted line: M^{ap}, grey line and disks: $M^{a\mu}$, light grey solid line: P.

the dominant fluctuation production is due to forces on the particle surfaces. What we find instead is a lower fluctuation intensity, and this is likely due to the smaller scales introduced into the flow by the smaller particles. This leads to increased dissipation, and this increase is stronger than the increase of production.

The generation and dissipation of fluctuating kinetic energy is governed by seven terms in Eq. (2.7). Understanding the relative importance of these terms is essential if we want to model the evolution of k. To this end, we examine the production and dissipation terms in one of our simulations. Figure 5 shows the source terms of k for case VI at $(t-t_0)/\tau_L = 1$ and 2, non-dimensionalised by $\mathcal{P} = \rho_{\mathrm{IS}}\widetilde{K}_{\mathrm{IS}}u_{\mathrm{IS}}/D_{\mathrm{p}}$. Clearly, A, the production due to the pressure on the particles is the dominant term, while B, Π and ε are also important. Figure 5(b) shows the source terms at $(t-t_0)/\tau_L = 2$, at which point the flow has established a quasi-steady regime, where the streamwise distribution of the source terms do not vary much in time. Terms A, B and Π are roughly constant over $0.1 < x/L < 0.80$, and ε is slightly increasing in magnitude over this region. In the region close to the downstream edge of the particle cloud, the relative importance of the source terms change quite significantly. The production term due to Reynolds stresses attains a higher magnitude than all the other source terms except A, primarily due to the transition to supersonic flow which significantly increases the streamwise velocity. We observe that A and Π are negatively correlated, and we find that the Pearson correlation coefficient for A and Π averages above 0.8 for all the simulations, and is strongest for the highest values of r.

4. 1D simulations

In this section, we consider 1D simulations of a Mach 2.6 shock wave impacting on a particle cloud with volume fraction $\alpha_{\mathrm{p}} = 0.1$ and particle number density of 763.9 mm^{-3}, i.e. case VII. As a baseline, we consider the most basic version of Eqs. (2.4)-(2.6) where all unclosed terms are set to zero. The computational domain is discretized into 1920 control volumes and extends from $x/L = -5/3$ to $x/L = 10/3$. The volume fraction field is generated by seeding 16000 particles uniformly over $0 \leq x/L \leq 1$, and the control volume height and width are chosen to match the desired volume fraction. Since the control volume length does not match exactly an integer number of particle separations there

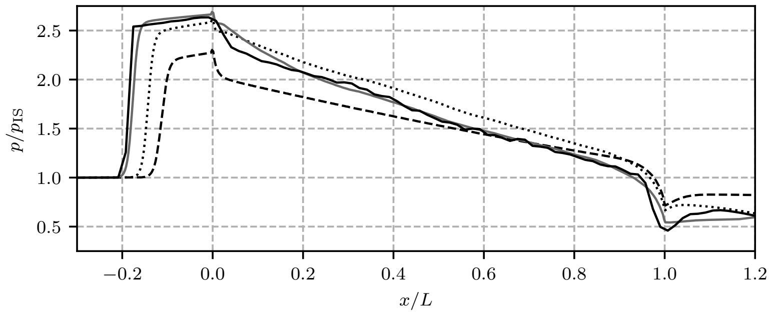

FIGURE 6. Pressure at $(t-t_0)/\tau_L = 1.5$ for case VII (solid line) and corresponding 1D simulations. No sub-grid closures and Clift & Gauvin's drag law: dashed line, no sub-grid closures and exact drag law: dotted line, sub-grid closures and exact drag law: solid grey line.

are small variations in the local volume fraction through the particle cloud. Although the particles are locked in space, the choice of drag law affects the flow through the appearance of the particle forces in the momentum equation. The force due to drag on each particle is applied only to the control volume containing the particle. We include the quasi-steady drag force and the Archimedes force on each particle. The quasi-steady drag is computed from the drag law of Clift and Gauvin, as cited in Schwarzkopf *et al.* (2011), where the drag coefficient is

$$C_{\text{d}} = \frac{24}{Re_{\text{p}}}\left[1.0 + 0.15Re_{\text{p}}^{0.687} + 0.0175Re_{\text{p}}(1 + 4.25\times 10^4 Re_{\text{p}}^{-1.16})^{-1}\right]. \tag{4.1}$$

Figure 6 shows the pressure from the 3D- and 1D-simulation at $(t-t_0)/\tau_L = 1.5$. We note that the basic wave-structure is the same in both cases, c.f. Figure 2. However, there are a number of differences between the 3D and 1D results. The reflected shock wave can be seen to be much stronger in the 3D case, and as a result its location is much further upstream than the reflected shock in the 1D case. We see that at $x/L = 0$ the pressure begins to decrease with x, sharply at first and then more slowly, with a constant negative gradient, over most of the cloud length. The 1D simulation shows a too steep and narrow initial pressure gradient, followed by a too weak constant pressure gradient region. At the downstream end of the particle cloud the 1D simulation does show an expansion region, but it is less pronounced than its 3D counterpart. Since the reflected shock is too weak, the transmitted shock is too strong, and we find elevated pressure levels downstream of the particle cloud.

We now demonstrate the effect of a few improvements to the simple 1D model. As a first iteration, we replace the drag law by a curve fit of the forces exerted on the particles in the 3D simulation. We refer to this approach as using an exact drag law. As can be seen in Figure 6, the resulting pressure distribution is much closer to the 3D simulation data than the results with Clift & Gauvin's drag law. We note that the pressure within the particle layer is quite a bit higher than it should be, but the gradient matches the 3D data well. The difference originates at the upstream edge of the particle cloud, where the 3D data has a rapid drop in pressure. Downstream we see the same problem as with the previous drag law. The pressure drop in the expansion region is not strong enough, but we see that the pressure even further downstream is now closer to the 3D data.

Finally, we include the sub-grid scale fluctuating kinetic energy and propose closures for R_{00}, P, A, B, Π and ε. We emphasise that these closures are specific to this case and are not recommended for general uses. Terms M^p and M^μ are neglected, as are all the transport terms labeled $D^{(\cdot)}$. R_{00} is closed by specifying the turbulence anisotropy, which we observe from the data to give roughly $R_{00} = 6k/5$. A and B are closed by the drag law. Π was found to be significantly correlated with the forces on the particles, and we set it simply to $\Pi = -0.3(A + B)$. For ε, we use a simple length scale model so that

$$\varepsilon = \frac{\rho k^{3/2}}{l}, \tag{4.2}$$

where l is the dissipation length scale. We use the 3D data to estimate the dissipation length scale, and as a first approach use a constant value of 10^{-4} m, i.e. slightly larger than the particle diameter. The resulting pressure distribution is shown in Figure 6. Clearly, the additional terms bring the simulation closer to the 3D data. The reflected shock is now well represented, and the distribution throughout the particle cloud is very good. There are still deviations close to the upstream and downstream edges of the particle cloud, but these are smaller than for the other two models.

Based on experimentation with different closures for the various unclosed terms in Eqs. (2.4)-(2.6) and the drag-law, we make the following observations;

(I) The drag law is important for the strength of the reflected shock. A stronger drag imposes a stronger force on the gas phase, in addition to increasing the production of fluctuating kinetic energy. We believe that capturing the initial spike in the drag coefficient is important for obtaining a correct reflected shock strength. Commonly applied drag-laws, including the one used here, does not capture this spike. Other studies that have investigated particle drag in the shock-particle cloud setting, e.g. Mehta *et al.* (2016, 2018), are therefore very important for simulation of these problems.

(II) The level of the fluctuating kinetic energy has an appreciable impact on the pressure field when it is computed from the total energy and kinetic energy fields, which is the most common solution method for both the Euler and Navier-Stokes equations. Neglecting the fluctuating kinetic energy leads to erroneous pressure gradients, and thus wrong mean flow.

(III) The Reynolds stress contribution in the momentum equation is significant. It affects the strength of the reflected shock wave, and in turn all the fields downstream. By tuning the anisotropy of the Reynolds stress tensor, we can to some extent adjust the reflected shock strength and the mean field profiles throughout the particle layer. A proper model for the Reynolds stress is thus necessary.

5. Conclusions

We have conducted three-dimensional resolved simulations of shock waves passing through particle clouds for varying Mach numbers, particle number densities and volume fractions. We investigated the bulk effect of the particle cloud and fitted power laws for the transmitted shock and reflected shock wave Mach numbers. We have also investigated the development of fluctuating kinetic energy, and found that it reaches values as high as two thirds of the local mean kinetic energy. The primary source of fluctuating kinetic energy is the forces on the particles, and both viscous dissipation and pressure-dilatation are significant sinks. We performed 1D simulations, corresponding to one of the 3D simulations, and demonstrated that a naive approach which ignores the unresolved fluctuations has several problems. Adding the exact drag law, taken from the 3D data, significantly improved the 1D simulations, but this approach still does not reproduce the 3D data very well. We included the fluctuating kinetic energy equation, provided closures for its sources and sinks, and the results from this extended equation set were significantly improved compared to the previous 1D simulations. The remaining deviations from the 3D data were located close to the upstream and downstream edge of the particle cloud.

Acknowledgments

The authors acknowledge use of computational resources from the Certainty cluster awarded by the National Science Foundation to CTR. The authors would like to thank Prof. Lele and Dr. Horwitz for interesting discussions.

REFERENCES

Bres, G. A., Bose, S. T., Emory, M., Ham, F. E., Schmidt, O. T., Rigas, G. & Colonius, T. 2018 Large-eddy simulations of co-annular turbulent jet using a Voronoi-based mesh generation framework. In *2018 AIAA/CEAS Aeroacoustics Conference*, p. 3302.

Hosseinzadeh-Nik, Z., Subramaniam, S. & Regele, J. D. 2018 Investigation and quantification of flow unsteadiness in shock-particle cloud interaction. *Int. J. Multiph. Flow* **101**, 186–201.

Houim, R. W. & Oran, E. S. 2016 A multiphase model for compressible granular–gaseous flows: formulation and initial tests. *J. Fluid Mech.* **789**, 166–220.

Lhuillier, D., Chang, C.-H. & Theofanous, T. G. 2013 On the quest for a hyperbolic effective-field model of disperse flows. *J. Fluid Mech.* **731**, 184–194.

Ling, Y., Wagner, J. L., Beresh, S. J., Kearney, S. P. & Balachandar, S. 2012 Interaction of a planar shock wave with a dense particle curtain: Modeling and experiments. *Phys. Fluids* **24**, 113301.

McGrath, T. P., Clair, J. G. S. & Balachandar, S. 2016 A compressible two-phase model for dispersed particle flows with application from dense to dilute regimes. *J. Appl. Phys.* **119**, 174903.

Mehta, Y., Neal, C., Jackson, T. L., Balachandar, S. & Thakur, S. 2016 Shock interaction with three-dimensional face centered cubic array of particles. *Phys. Rev. Fluids* **1**, 054202.

Mehta, Y., Neal, C., Salari, K., Jackson, T. L., Balachandar, S. & Thakur, S. 2018 Propagation of a strong shock over a random bed of spherical particles. *J. Fluid Mech.* **839**, 157–197.

Regele, J. D., Rabinovitch, J., Colonius, T. & Blanquart, G. 2014 Unsteady effects in dense, high speed, particle laden flows. *Int. J. Multiph. Flow* **61**, 1–13.

Schwarzkopf, J. D. & Horwitz, J. A. 2015 The BHR equations re-derived with immiscible particle effects. Los Alamos National Laboratory.

Schwarzkopf, J. D., Sommerfeld, M., Crowe, C. T. & Tsuji, Y. 2011 *Multiphase Flows with Droplets and Particles*. CRC Press.

Theofanous, T. G. & Chang, C.-H. 2017 The dynamics of dense particle clouds subjected to shock waves. Part 2. Modeling/numerical issues and the way forward. *Int. J. Multiph. Flow* **89**, 177–206.

Theofanous, T. G., Mitkin, V. & Chang, C.-H. 2016 The dynamics of dense particle clouds subjected to shock waves. Part 1. Experiments and scaling laws. *J. Fluid Mech.* **792**, 658–681.

Theofanous, T. G., Mitkin, V. & Chang, C.-H. 2018 Shock dispersal of dilute particle clouds. *J. Fluid Mech.* **841**, 732–745.